

A barotropic model of eddy saturation

NAVID C. CONSTANTINOU*

Scripps Institution of Oceanography, University of California, San Diego, La Jolla, California

ABSTRACT

“Eddy saturation” refers to a regime in which the total mass transport of an oceanic current is insensitive to the wind stress strength. Baroclinicity is currently believed to be key to the development of an eddy-saturated state. Here, we show that eddy saturation occurs in a barotropic flow over topography, without baroclinicity. We show that eddy saturation is a fundamental property of barotropic dynamics above topography. We demonstrate that the main factor controlling the appearance or not of eddy-saturated states is the structure of geostrophic contours, that is the contours of the ratio of the Coriolis parameter over the ocean’s depth. Eddy-saturated states occur when the geostrophic contours are *open*, that is when the geostrophic contours span the whole zonal extent of the domain. We demonstrate this minimal requirement for eddy-saturated states in a scenario relevant to the Antarctic Circumpolar Current using numerical integrations of a single-layer quasi-geostrophic flow over two different topographies characterized by either open or closed geostrophic contours. We also extend the stability method of Hart [*J. Atmos. Sci.*, **36**, 1736–1746, (1979)] to explain the flow transitions that occur in the solutions with open geostrophic contours.

1. Introduction

The Antarctic Circumpolar Current (ACC) is a key element of the climate system. The ACC is driven by a combination of strong westerly winds and buoyancy forcing. Straub (1993) advanced the remarkable hypothesis that the equilibrated ACC zonal transport should be insensitive to the strength of the wind stress forcing. This insensitivity was later verified in eddy resolving ocean models of the Southern Ocean and is now referred to as *eddy saturation* (Hallberg and Gnanadesikan 2001; Tansley and Marshall 2001; Hallberg and Gnanadesikan 2006; Hogg et al. 2008; Farneti et al. 2010; Meredith et al. 2012; Morisson and Hogg 2013; Munday et al. 2013; Abernathey and Cessi 2014; Farneti et al. 2015). A second defining feature of eddy saturation is that, even though the total ACC transport changes very little, the eddy kinetic energy (EKE) is approximately linearly related to the wind stress.

Some indications of eddy saturation are seen in observations (Böning et al. 2008; Firing et al. 2011). Moreover, there is evidence that the strength of the westerly winds over the Southern Ocean, which force the ACC, are increasing (Thompson and Solomon 2002; Marshall 2003; Yang et al. 2007; Swart and Fyfe 2012). Recently, Hogg et al. (2015) using satellite altimetry data identified (*i*) a linear trend of the Southern Ocean surface EKE and also

(*ii*) found that the ACC zonal transport remains insensitive or even decreasing. Thus, Hogg et al. (2015) concluded that the ACC is in an eddy saturated state. Understanding the mechanisms behind eddy saturation is particularly relevant given the strengthening of the Southern Ocean winds over the last decades, and the potential enhanced strengthening under global warming forcing (Bracegirdle et al. 2013). The question that naturally arises is how will the ACC transport respond to increasing winds?

All previous investigations of eddy saturation, starting with Straub (1993), and continuing with the detailed models of Nadeau and Straub (2009, 2012); Nadeau et al. (2013) and Nadeau and Ferrari (2015), have emphasized the role of baroclinic processes in eddy saturation. Recently, Marshall et al. (2017) and Mak et al. (2017) showed that eddy saturation might emerge as a result of an eddy flux parametrization that was introduced by Marshall et al. (2012). In agreement with Straub (1993), Marshall et al. (2017) relate the production of EKE to the vertical shear of the zonal mean flow. Baroclinic instability is identified as the main source of EKE in all of these explanations of eddy saturation.

According to Johnson and Bryden (1989) different density layers are coupled via interfacial form stress that transfers momentum downwards from the sea-surface to the bottom. But at the bottom it is topographic form stress that transfers momentum from the ocean to the solid earth (Munk and Palmén 1951). Thus, a main question concerning eddy saturation is how can the total vertically integrated transport be insensitive to applied wind stress,

*Corresponding author address: Navid C. Constantinou, Scripps Institution of Oceanography, University of California San Diego, La Jolla, CA 92093-0213, USA.

E-mail: navid@ucsd.edu

while the topographic form stress always balances most of the applied wind stress? In considering this question note that it is only the *standing* eddies that result in time-mean topographic form stress. Arguments about the growth rate of transient baroclinic eddies based on the slope of buoyancy surfaces seem irrelevant to the strength of the standing eddies, and the pressure–slope correlation that produces the topographic form stress to balance the wind stress. [Abernathy and Cessi \(2014\)](#) showed that isolated topographic features result in localized absolute baroclinic instability located over the topography and an associated almost-barotropic standing wave pattern. Transient eddies are suppressed away from the topography and, relative to the flat-bottom case, the thermocline is shallow and isopycnal slopes are small. Thus arguments assuming that the isopycnal slopes are so steep as to be marginal with respect to the flat-bottomed baroclinic instability cannot explain eddy saturation in this model configuration with localized topography. In this paper we emphasize the role of the standing eddies, and their form stress, in determining transport in an eddy saturated regime in a barotropic setting.

Indeed, lately there has been increasing evidence arguing for the importance of the barotropic mechanisms in determining the ACC transport. [Ward and Hogg \(2011\)](#) used a 5-layer primitive equation wind-driven model with an ACC-type configuration starting from rest. Following turn-on of the wind a strong barotropic current forms within several days that is able to transfer most of the imparted momentum to the bottom; only after several years does the momentum start being transferred vertically via interfacial form stress. The fast response is that a bottom pressure signal arises a few days after turn-on, and the associated topographic form stress couples the ocean to the solid earth. Subsequently, for about ten years, and contrary to the statistical equilibrium scenario described by [Johnson and Bryden \(1989\)](#), interfacial form stress transfers momentum vertically from the bottom *upwards*. In addition, [Thompson and Naveira Garabato \(2014\)](#) also emphasized the role of the barotropic component of the flow and that of the standing eddies (or standing meanders) in setting up the momentum balance and ACC transport. Furthermore, studies using in situ velocity measurements, satellite altimetry, and output from the Southern Ocean State Estimate (SOSE) also argue in favor of the importance of the barotropic component of the ACC ([Rintoul et al. 2014](#); [Peña Molino et al. 2014](#); [Masich et al. 2015](#); [Donohue et al. 2016](#)).

[Constantinou and Young \(2016\)](#) discussed the role of standing eddies using the simplest barotropic model forced by an imposed steady wind stress and retarded by a combination of bottom drag and topographic form stress ([Hart 1979](#); [Davey 1980](#); [Holloway 1987](#); [Carnevale and Frederiksen 1987](#)). [Constantinou and Young \(2016\)](#) used a random monoscale topography and argued that a critical requirement for eddy saturation is that the geostrophic contours (that is the contours of the planetary plus the topographic

contribution to potential vorticity) are open in the zonal direction. A main goal of the present paper is to show that eddy saturation occurs with simple topography, provided the geostrophic contours are open in the direction of the large-scale current.

We show that this barotropic model with simple deterministic topography and without baroclinic instability, can exhibit impressive eddy saturation provided that the geostrophic contours are open: the model shows both insensitivity of the zonal transport to the increase of wind stress forcing and also linear increase of EKE with wind stress forcing. In this model, transient eddies arise as an instability due to the interaction of the large-scale zonal flow with the topography. These transient barotropic eddies have scales comparable to, or smaller than, those imposed by the topography and might be confounded with deformation-scale baroclinic eddies.

2. Setup

Consider the quasi-geostrophic dynamics of a barotropic fluid of depth $H - h(x, y)$ on a beta-plane with the fluid velocity consisting of a large-scale domain-averaged zonal flow, $U(t)$, along the zonal x direction plus smaller-scale eddies with velocity (u, v) . The eddy component of the flow is derived via an eddy streamfunction $\psi(x, y, t)$ as $(u, v) = (-\psi_y, \psi_x)$; the streamfunction of the total flow is $-U(t)y + \psi(x, y, t)$. The relative vorticity is $\nabla^2 \psi$, where $\nabla^2 \stackrel{\text{def}}{=} \partial_x^2 + \partial_y^2$, and the quasi-geostrophic potential vorticity (QGPV) of the flow is

$$f_0 + \beta y + \eta + \nabla^2 \psi. \quad (1)$$

In (1), f_0 is the Coriolis parameter in the center of the domain, β is the meridional planetary vorticity gradient and $\eta(x, y) \stackrel{\text{def}}{=} f_0 h(x, y)/H$ is the topographic contribution to QGPV or simply the *topographic PV*. The QGPV and the large-scale flow evolve through:

$$\nabla^2 \psi_t + J(\psi - Uy, \nabla^2 \psi + \eta + \beta y) + D \nabla^2 \psi = 0, \quad (2a)$$

$$U_t = F - \mu U - \langle \psi \eta_x \rangle, \quad (2b)$$

([Hart 1979](#); [Davey 1980](#); [Holloway 1987](#); [Carnevale and Frederiksen 1987](#)). In (2a) J is the Jacobian, $J(a, b) \stackrel{\text{def}}{=} a_x b_y - a_y b_x$, and $D \stackrel{\text{def}}{=} \mu + v_4 \nabla^4$ is the dissipation operator which includes linear Ekman drag μ and hyperviscosity v_4 used for numerical stability. On the right of (2b), $\langle \psi \eta_x \rangle$ is the topographic form stress, with angle brackets denoting an average over the (x, y) -domain. The large-scale flow $U(t)$ in (2b) is forced by the constant $F = \tau / (\rho_0 H)$, where τ is the uniform surface wind stress and ρ_0 is the reference density of the fluid, while being retarded by a combination of bottom drag and topographic form stress.

The domain is periodic in both the zonal and the meridional directions, with size $2\pi L \times 2\pi L$. The role of hyperviscosity is limited only to the removal of small-scale vorticity.

Thus the hyperviscosity has a very small effect on larger scales and energy dissipation is mainly due to drag μ .

The model formulated in (2) is the simplest model that can be used to investigate beta-plane turbulence above topography driven by a large-scale zonal wind stress applied at the surface of the fluid. It has been used in the past for studying the interaction of zonal flows with topography (Hart 1979; Davey 1980; Holloway 1987; Carnevale and Frederiksen 1987) and recently by Constantinou and Young (2016) for studying the geostrophic flow regimes above random monoscale topography.

Inspired by the Southern Ocean we take $L = 775$ km, $H = 4$ km, $\rho_0 = 1035 \text{ kg m}^{-3}$, $f_0 = -1.26 \times 10^{-4} \text{ s}^{-1}$ and $\beta = 1.14 \times 10^{-11} \text{ m}^{-1} \text{s}^{-1}$. Also, we take $h_{\text{rms}} \stackrel{\text{def}}{=} \sqrt{\langle h^2 \rangle} = 200$ m, which implies that $\eta_{\text{rms}} = 6.3 \times 10^{-6} \text{ s}^{-1}$. For Ekman drag we use $\mu = 6.3 \times 10^{-8} \text{ s}^{-1} \approx (180 \text{ day})^{-1}$ (Arbic and Flierl 2004).

Results are reported using two sinusoidal topographies:

$$\eta^{\parallel} = \sqrt{2}\eta_{\text{rms}} \cos(14x/L), \quad (3a)$$

$$\eta^{\times} = 2\eta_{\text{rms}} \cos(10x/L) \cos(10y/L). \quad (3b)$$

Both topographies (3) are monoscale, that is they are characterized by a single length-scale $\ell_{\eta} = \sqrt{\langle \eta^2 \rangle / \langle |\nabla \eta|^2 \rangle}$, which is:

$$\ell_{\eta} \approx \ell_{\eta}^{\times} = 0.071L = 55.03 \text{ km}.$$

An important factor controlling the behavior of the flow turns out to be the geostrophic contours, that is the level sets of $\beta y + \eta(x, y)$. Figure 1 shows the structure of geostrophic contours for the two topographies η^{\parallel} and η^{\times} using the parameters given above. Here, we distinguish between “open” and “closed” geostrophic contours: open geostrophic contours span the full zonal extend of the domain; see for example the two contours marked with thick black curves in figure 1. For any nonzero β , all geostrophic contours for topography η^{\parallel} are open while for topography η^{\times} there exist both closed as well as open geostrophic contours. However, for topography η^{\times} open geostrophic contours, such as the one shown in figure 1(b), are only found in the vicinity of narrow channels that span the horizontal extend of the domain snaking around local maxima and minima of $\beta y + \eta^{\times}$. We say, therefore, that η^{\times} is characterized by closed geostrophic contours.

It is useful to decompose the eddy streamfunction ψ into time-mean “standing eddies” with streamfunction $\bar{\psi}$, and residual “transient eddies” ψ' , so that:

$$\psi(x, y, t) = \bar{\psi}(x, y) + \psi'(x, y, t),$$

where the time-mean is $\bar{\psi} \stackrel{\text{def}}{=} \lim_{T \rightarrow \infty} \frac{1}{T} \int_{t_0}^{t_0+T} \psi(x, y, t') dt'$, with t_0 the time the flow needs to reach a statistically steady state. Similarly, all fields can then be decomposed into time-mean and transient components e.g., $U(t) = \bar{U} + U'(t)$.

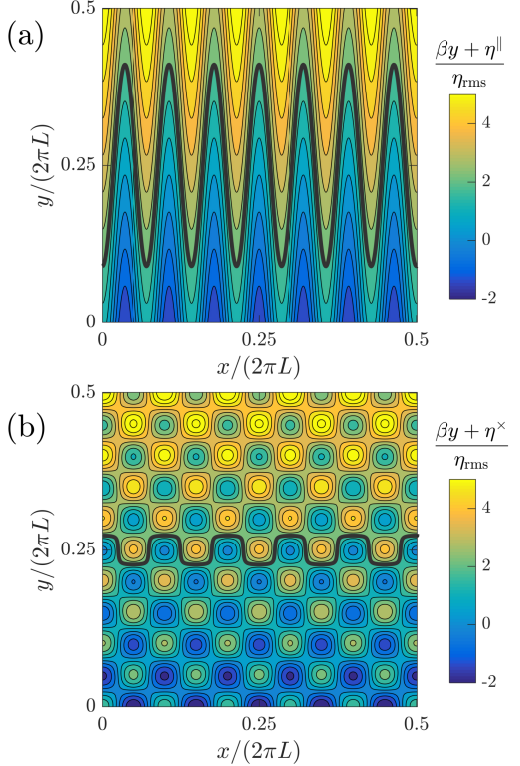


FIG. 1. The structure of the geostrophic contours, $\beta y + \eta$, for the two types of topographies used in this paper: panel (a) uses η^{\parallel} and panel (b) uses η^{\times} . For both cases $\beta \ell_{\eta} / \eta_{\text{rms}} = 0.1$. An open geostrophic contour for each case is marked with a thick curve. The case $\beta y + \eta^{\parallel}$ consists of only open geostrophic contours while $\beta y + \eta^{\times}$ consists of mostly closed ones. (Only a quarter of the flow domain is shown.)

We are interested in how the time-mean large-scale flow \bar{U} , which is directly related to the time-mean total zonal transport, depends on wind stress forcing F .

3. Results

We report results from numerical solutions of (2) for the two topographies in (3). All solutions presented employ 512^2 grid points; we have verified that results remain qualitatively unchanged when doubling the resolution. The hyperviscosity coefficient is set to $v_4 = 2.27 \times 10^9 \text{ m}^4 \text{ s}^{-1}$. The system is evolved using the Exponential Time Differencing 4th-order Runge-Kutta time-stepping scheme (Cox and Matthews 2002; Kassam and Trefethen 2005). Time-averaged quantities are calculated by averaging the fields over the interval $30 \leq \mu t \leq 60$.

a. Variation of the time-mean large-scale flow with wind stress forcing

Figure 2 shows how the time-mean large-scale flow \bar{U} varies with wind stress forcing F for the two topographies.

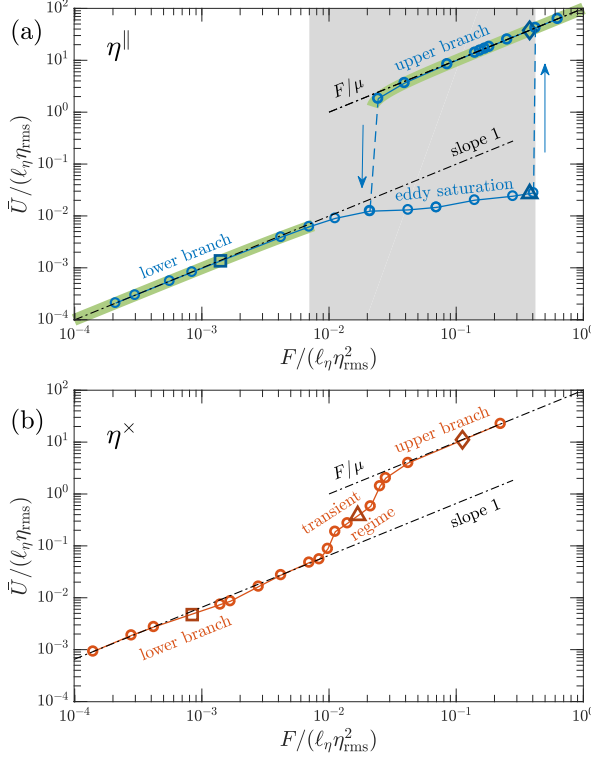


FIG. 2. The equilibrated time-mean large-scale flow \bar{U} as a function of the non-dimensional forcing for the two topographies. Panel (a) shows the case with open geostrophic contours while panel (b) shows the case with closed geostrophic contours. Dash-dotted lines mark the slope 1 and the time-mean large-scale flow $\bar{U} = F/\mu$. In panel (a) the eddy saturation regime $7.0 \times 10^{-3} \leq F/(\ell_\eta \eta_{\text{rms}}^2) \leq 4.1 \times 10^{-1}$ is shaded. The thick semitransparent green curve marks the stability region of the steady solution (7). The points marked with a square \square , a triangle \triangle and a diamond \diamond correspond to the three typical cases for which the energy spectra and flow field snapshots are shown in figures 4 and 5.

A generic feature that characterizes both topographies used here (as well as other more complex and/or multiscale topographies) is the following: as wind stress strength varies from weak to stronger values the flow transitions from a regime with relatively small time-mean large-scale flow \bar{U} to a regime with large \bar{U} . Specifically, for high wind stress forcing values the time-mean large-scale flow becomes $\bar{U} \approx F/\mu$, which is the maximum value for \bar{U} in the absence of topography (see (2b)). These two regimes are referred to as the lower-branch and the upper-branch (Davey 1980), and are indicated in figure 2. In both branches, the flow reaches a steady state without any transients, after an initial adjustment on the time scale of $O(\mu^{-1})$. For intermediate wind stress forcing values the flow develops transients.

In the rest of this subsection we describe in detail the qualitative features of the flow in the lower and upper

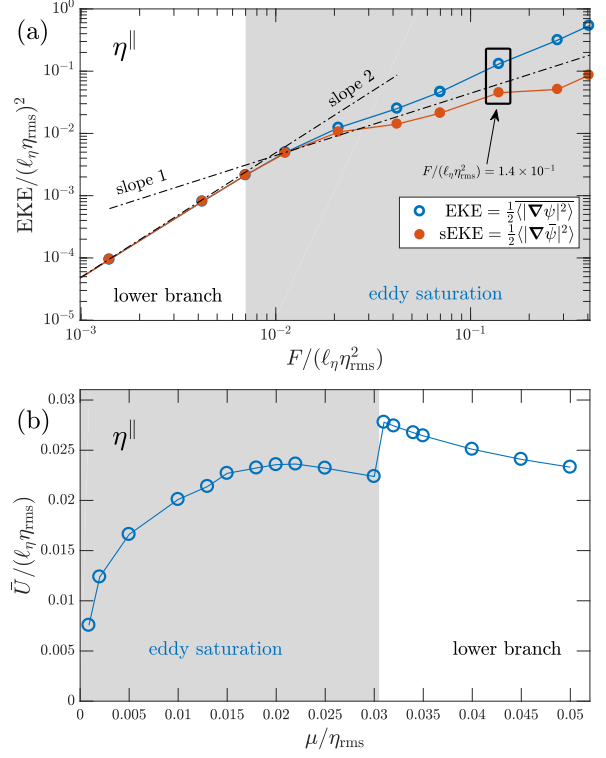


FIG. 3. Panel (a) shows how the equilibrated EKE and the standing wave EKE (sEKE) vary with wind stress forcing for the topography η^\parallel , as the flow transitions from the lower-branch to the eddy saturation regime. Dash-dotted lines mark the slopes 1 and 2. Panel (b) shows how the equilibrated time-mean large-scale flow \bar{U} varies with bottom drag μ in the eddy saturation regime. For these experiments wind stress forcing is kept constant at $F/(\ell_\eta \eta_{\text{rms}}^2) = 1.4 \times 10^{-1}$ (highlighted in panel (a)) while bottom drag μ varies.

branches, as well as the transition from one branch to the other for the two topographies.

For weak wind stress forcing F values (i.e. in the lower branch) the equilibrated solutions of (2) are time-independent without any transient eddies. These steady states have both a large-scale flow U and an associated stationary eddy flow field ψ that vary linearly with wind stress forcing F . As a result, EKE varies quadratically with wind stress, as F^2 . Figure 3(a) shows the variation of EKE with wind stress forcing for topography η^\parallel and confirms the F^2 dependence in the lower branch (similar behavior is found for topography η^\times ; not shown). As the wind stress increases beyond a certain value the lower-branch steady states undergo an instability and begin to develop transients. The onset of this instability is roughly at $F/(\ell_\eta \eta_{\text{rms}}^2) \approx 7 \times 10^{-3}$ for both topographies. (The stability of the lower-branch states for topography η^\parallel is studied in section 4.)

However, for wind stress forcing values beyond the threshold of the lower-branch instability the flow above the two topographies are qualitatively different; for example, topography η^{\parallel} shows eddy saturation while topography η^{\times} does not.

For topography η^{\parallel} , as wind stress continues to increase beyond the onset of the transient eddy instability, the time-mean large-scale flow \bar{U} ceases to grow linearly with F ; instead \bar{U} grows at a much slower rate. In fact, \bar{U} shows only a very weak dependence on wind stress strength in the shaded region of figure 2(a): \bar{U} increases only about 4-fold in the course of a 60-fold wind stress increase from $F/(\ell_{\eta} \eta_{\text{rms}}^2) = 7.0 \times 10^{-3}$ up to 4.1×10^{-1} . This regime is identified as the *eddy saturation regime*. Figure 3(a) shows that in the eddy saturation regime the EKE varies with wind stress forcing at a rate much slower than quadratic. It is also apparent from figure 3(a) that strong transient eddies characterize the eddy saturation regime; this can be seen by the diminishing of the standing wave EKE (sEKE), that is the EKE that results from the standing waves alone.

The barotropic model (2) predicts that for a fully eddy-saturated state EKE should vary linearly with wind stress forcing, merely as a consequence of the energy power integral: $\langle -\psi \times (2a) \rangle$ gives:

$$\bar{U} \langle \bar{\psi} \eta_x \rangle + \underbrace{\bar{U}' \langle \psi' \eta_x \rangle}_{\text{negligible}} = 2\mu \underbrace{\langle \frac{1}{2} |\nabla \psi|^2 \rangle}_{\stackrel{\text{def}}{=} \text{EKE}} + \underset{\text{small hyperviscous dissipation}}{\dots} . \quad (4)$$

If \bar{U} does not vary with F , then (2b) implies that the form stress $\langle \bar{\psi} \eta_x \rangle$ varies linearly with F and thus (4) implies that EKE also varies linearly with F .

Recently, Marshall et al. (2017), using a primitive equations model, showed that increase in bottom drag results in increasing ACC transport. Here, we show that the barotropic model (2) shows similar behavior in the eddy saturation regime. Figure 3(b) shows how the time-mean large-scale flow \bar{U} varies when wind stress forcing is kept fixed at $F/(\ell_{\eta}^2 \eta_{\text{rms}}^2) = 1.4 \times 10^{-1}$ while bottom drag μ changes: \bar{U} increases with μ . Within model (2) this is easily rationalized: large bottom drag damps the eddy field ψ , thereby decreasing the form stress. Hence, increased bottom drag strengthens the time-mean large-scale flow \bar{U} , which is necessary to balance the wind stress forcing F in the eddy saturation regime. However, if we increase bottom drag μ beyond a certain threshold the flow ceases to be turbulent and transitions from the eddy saturation regime to the lower-branch solution (for the case in figure 3(b) this transition occurs at $\mu/\eta_{\text{rms}} = 3 \times 10^{-2}$). On the lower-branch the time-mean large-scale flow \bar{U} decreases with increasing μ .

The eddy saturation regime terminates at $F/(\ell_{\eta} \eta_{\text{rms}}^2) \approx 4.1 \times 10^{-1}$ by a discontinuous transition to the upper-branch, marked with a dashed line in figure 2(a). The upper branch steady solutions are characterized by much larger values of time-mean large-scale flow \bar{U} compared

to ones in the eddy saturation regime or in the lower-branch. This discontinuous transition has been coined *drag crisis* (Constantinou and Young 2016). The location of the drag crisis exhibits hysteresis (Charney and DeVore 1979): as we increase wind stress forcing the drag crisis and the transition to the upper branch occurs at $F/(\ell_{\eta} \eta_{\text{rms}}^2) \approx 4.1 \times 10^{-1}$. However, if we initiate our model with the upper-branch solutions and start decreasing the wind stress forcing, we can find solutions in the upper branch down to $F/(\ell_{\eta} \eta_{\text{rms}}^2) \approx 2.44 \times 10^{-2}$: see figure 2(a). We note that one has to be very delicate in initiating the system appropriately to obtain these upper branch solutions. Thus, although the upper-branch solutions shown in figure 2(a) are linearly stable, their basin of attraction is much smaller than those of the co-existing eddy-saturated solutions. The extent of the region of multiple stable equilibria is explained by studying the stability of the upper-branch solution (see section 4).

On the other hand, the case with topography with closed geostrophic contours η^{\times} in figure 2(b), does not exhibit any drag crisis nor any multiple equilibria. More importantly, topography η^{\times} does not show any eddy saturation regime; there is only a slight, barely noticeable, decrease from the linear growth of the time-mean large-scale flow \bar{U} with F ($8.0 \times 10^{-3} \leq F/(\ell_{\eta} \eta_{\text{rms}}^2) \leq 2.0 \times 10^{-3}$), and for those wind stress values the flow does not have any transient eddies. Transient eddies appear for wind stress forcing $F/(\ell_{\eta} \eta_{\text{rms}}^2) > 4.2 \times 10^{-3}$. For wind stress forcing values beyond the onset of transient eddies the flow transitions from the lower to the upper branch in a continuous manner between $F/(\ell_{\eta} \eta_{\text{rms}}^2) \approx 8.0 \times 10^{-2}$ and 4.2×10^{-2} .

b. The flow regimes

As described in the previous subsection, we distinguish three qualitatively different flow regimes for each topography. There exist, for both topographies, a lower-branch flow regime for weak wind stress forcing and an upper-branch flow regime for strong wind stress forcing. These flow regimes consist of steady flows without any transient eddies. In between the lower- and upper-branch flow regimes there exists a regime in which the flow has a transient component: the “eddy saturation regime” for topography η^{\parallel} case and the “transient regime” for topography η^{\times} . These intermediate regimes are characterized by flows that feature strong transients and are turbulent, especially the eddy saturated case. Moreover, in these regimes the flow shows energy content in a wide range of spatial scales.

The eddy field ψ in the eddy saturated regime is characterized as two-dimensional turbulence. The wind F drives directly the large-scale flow U in (2b) and, in turn, U drives the eddy field through the term $U \eta_x$ in (2a). This is a direct transfer of energy from the largest possible scale to the

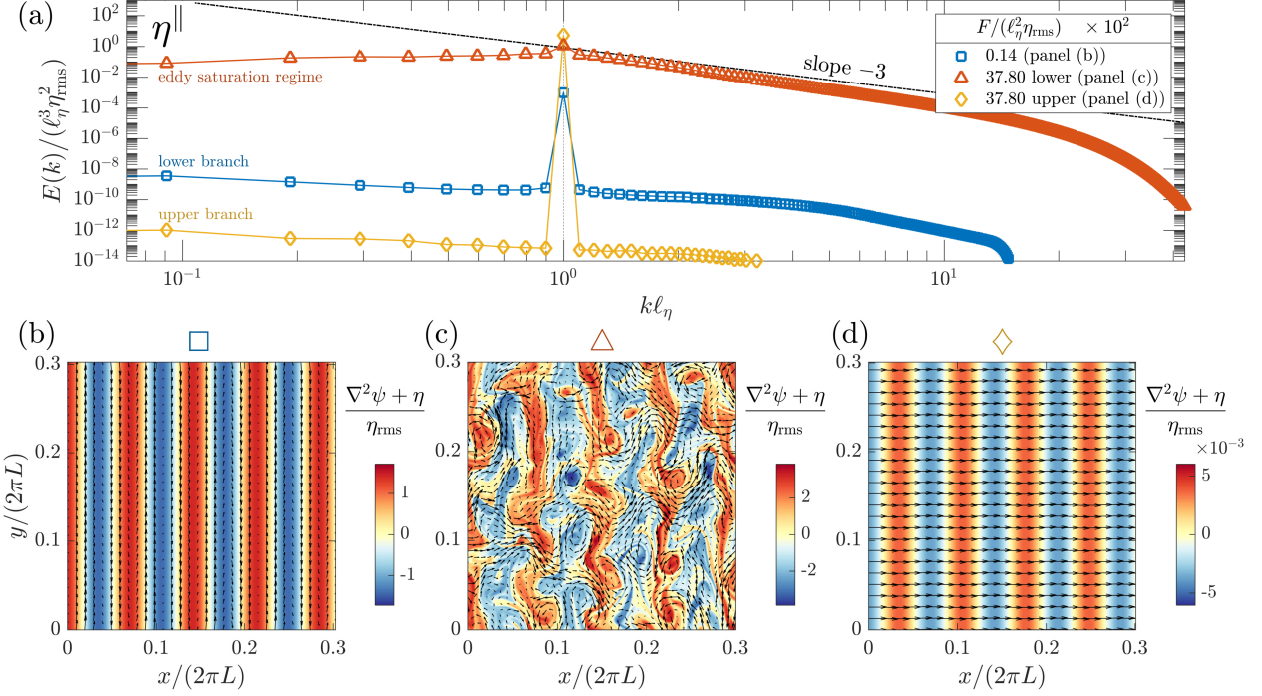


FIG. 4. Panel (a) shows the energy spectra for three typical cases using topography η^\parallel with open geostrophic contours. Panels (b) to (d) show a final snapshot of the sum of the relative vorticity with the topographic PV, $\nabla^2\psi + \eta$ (colors) overlayed with the total flow field ($U + u(x,y), v(x,y)$) for each of the cases presented in panel (a). (In panels (b)-(d) only a fraction of the flow domain is shown for better visualization.)

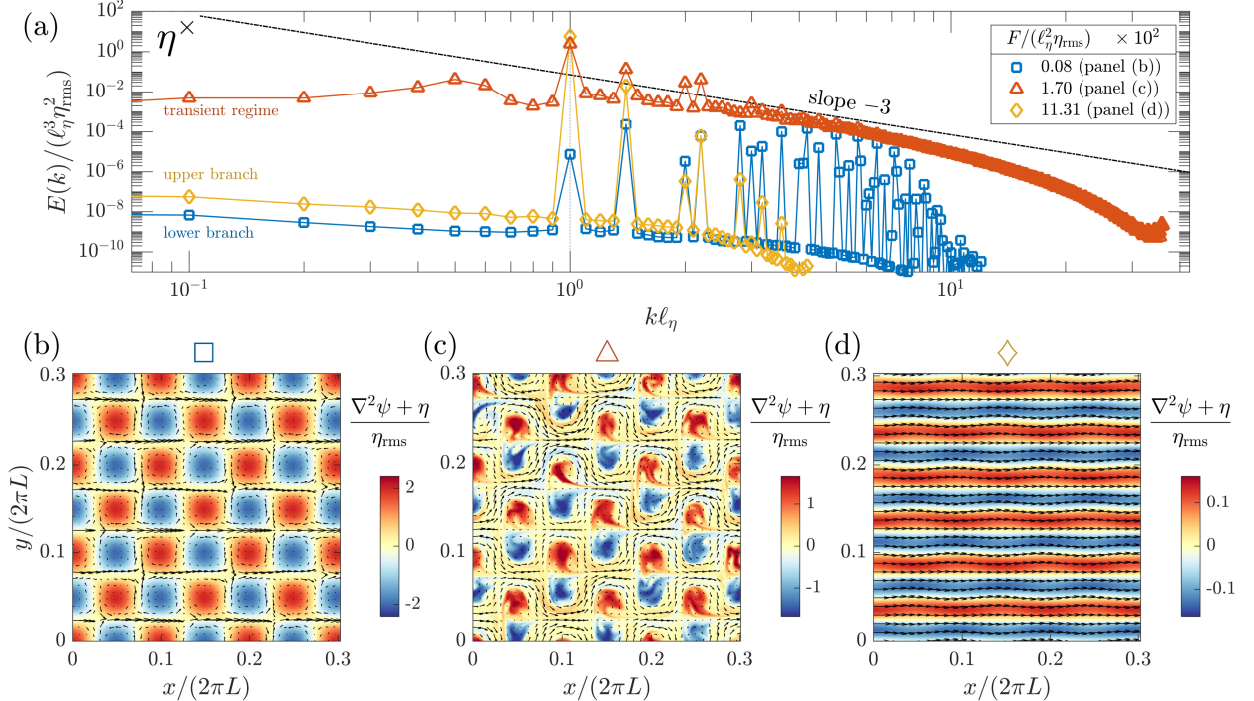


FIG. 5. Same as figure 4 but for three typical cases using topography η^\times with closed geostrophic contours.

eddies on the length scale of the topography ℓ_η . This turbulent regime is anisotropic; for example for the case marked with triangle in figure 2(a) and shown in figure 4(c) the transient eddy velocities are related by $\langle u^2 \rangle \approx 0.57 \langle v^2 \rangle$. The eddy flow exhibits energy and enstrophy inertial ranges. The enstrophy inertial range shows a spectral slope close to -3 , as predicted by homogeneous isotropic turbulence arguments. The energy inertial range produces an inverse transfer of energy from scales ℓ_η to larger scales. However, the energy inertial range does not show a spectral $-5/3$ slope; on the contrary there is a positive spectral slope.

Figures 4 and 5 show the energy spectra and a snapshot of the flow fields for a typical representative case of each of the three flow regimes (the cases presented in figures 4 and 5 are the ones marked with a square, a triangle and a diamond in panels (a) and (b) of figure 2). Characteristically, for the open geostrophic contours case (figure 4) the eddy saturated solution shows an energy content in spatial scales other than ℓ_η that is at least eight orders of magnitude larger compared to the steady lower- and upper-branch solutions. Similar behavior is seen for the closed geostrophic contours case of figure 5. The difference between these two cases is that for topography η^\times the lower- and upper- branch solutions are not monochromatic, i.e. they do not have power only at scale ℓ_η : the nonlinearity due to non-vanishing Jacobian term $J(\psi, \eta^\times)$ induces energy to cascade to scales smaller than scale ℓ_η that is directly forced by the topography.

4. The stability of the lower- and upper-branch solutions for topography η^\parallel

For topography of the form $\eta = \eta_0 \cos(mx)$ (as is (3a)) we can understand the transitions among the three flow regimes by studying a 3-dimensional invariant manifold of model (2). It is easy to verify in this case that there is a 3-dimensional invariant manifold by assuming that the eddy streamfunction is:

$$\psi(x, y, t) = [S(t) \sin(mx) + C(t) \cos(mx)] / m. \quad (5)$$

Inserting (5) in (2), and because the term $J(\psi, \eta)$ identically vanishes, equations (2) reduce to:

$$\frac{dC}{dt} = -\mu C + m(\beta/m^2 - U)S, \quad (6a)$$

$$\frac{dS}{dt} = -\mu S - m(\beta/m^2 - U)C - \eta_0 U, \quad (6b)$$

$$\frac{dU}{dt} = F - \mu U + \frac{1}{2} \eta_0 S, \quad (6c)$$

(after also ignoring v_4 in D). Steady equilibrium solutions of (6) can be found in the form:

$$U = U^e, \quad \psi(x, y) = \underbrace{[S^e \sin(mx) + C^e \cos(mx)] / m}_{\stackrel{\text{def}}{=} \psi^e}. \quad (7)$$

Both the lower- and upper- branch solutions for the case with topography η^\parallel are *exactly* such steady solutions in the form of (7); see panels (b) and (d) of figure 4. Hart (1979) studied the stability of solutions (7) to perturbations that lie within this invariant manifold. In the Appendix we study the stability of (7) to a general perturbation that may or may not lie within the invariant manifold. The region of stability of the lower- and upper- branch, as calculated in the Appendix, is marked in figure 2(a) with the thick solid green curve. Both the appearance of transient eddies as wind stress is increased, as well as the termination of the upper-branch solution as wind stress is decreased, are identified with the onset of an instability of the lower- and upper-branch solutions (7) respectively. Note though, that the lower-branch instability is first instigated by perturbations that lie outside the invariant manifold; stability to perturbations within the invariant manifold, as done by Hart (1979), predicts that the lower branch remains stable for wind stress forcing values up to three orders of magnitude larger than the value at which transient eddies do appear (see figure A1).

5. Discussion

The results reported here demonstrate that eddy saturation *does not* require baroclinicity, despite previous claims. A barotropic setting is capable of producing an eddy saturation regime with all three signature features, that is

- (i) transport is insensitive to wind stress forcing,
- (ii) EKE varies close to linearly rather than quadratically with wind stress forcing, and
- (iii) transport increases with increasing bottom drag.

The factor which controls the appearance or not of eddy saturated states is whether or not the geostrophic contours are open. Moreover, we have demonstrated that eddy saturation does not even require the presence of a “complex” topography. A y -independent topography that consist of a series of alternating meridional ridges, e.g. as is η^\parallel , suffices to produce eddy saturation.

For the y -independent topography with open geostrophic contours η^\parallel , we extended the stability analysis of Hart (1979) to encompass any general flow perturbations. Thus, we managed to identify the various flow transitions shown in figure 2(a) with the onset of an instability. The stability calculations presented in the Appendix crucially depend on that the topography η^\parallel does not depend on y . Moreover, the same flow transitions that occur above more complex topography $\eta(x, y)$ with open geostrophic contours result from the same instability.

The flow characteristics that were described in section 3 are not quirks of the simple sinusoidal topographies (3). The eddy saturation regime, the drag crisis, and multiple equilibria that are present here when geostrophic contours

are open, have been all also recently found to exist in this model for a flow above a random monoscale topography with open geostrophic contours (Constantinou and Young 2016). In addition, the same phenomena were found to exist with a multi-scale topography that has a k^{-2} power spectrum (not reported).

The results presented here emphasize the role of barotropic processes in eddy saturation. Even though the ACC is strongly affected by baroclinic processes, our results reinforce increasing evidence arguing for the importance of the barotropic mechanisms in determining the ACC transport (Ward and Hogg 2011; Thompson and Naveira Garabato 2014). We thus speculate that the role of standing eddies in setting up the barotropic component of the ACC transport through topographic form stress will be important even in a stratified multi-layered model that includes a large-scale barotropic flow.

Acknowledgments. I am mostly grateful to William Young for his support and his insightful comments. Discussions with Petros Ioannou, Spencer Jones, Sean Haney, Cesar Rocha, Andrew Thompson, Gregory Wagner and Till Wagner are greatly acknowledged. This project was supported by the NOAA Climate and Global Change Postdoctoral Fellowship Program, administered by UCAR's Cooperative Programs for the Advancement of Earth System Sciences. The MATLAB code used in this paper is available at the github repository: https://github.com/navidcy/QG_ACC_1layer.

APPENDIX

Stability of the invariant manifold steady state (7)

Assume perturbations about the steady state (7):

$$\begin{aligned} U(t) &= U^e + v(t), \\ \psi(x, y, t) &= \psi^e(x, y) + \phi(x, y, t) \\ &\quad + [s(t) \sin(mx) + c(t) \cos(mx)]/m. \end{aligned} \quad (\text{A1})$$

In (A1) we write the perturbation streamfunction as a sum of a perturbation that lies within the 3-state invariant manifold $[s \sin(mx) + c \cos(mx)]/m$, and a perturbation that does not project on the invariant manifold, ϕ . That said, ϕ satisfies: $\int \phi(x, y, t) e^{imx} dx dy = 0$.

By inserting (A1) in (2) and using that (7) is a solution of (6) we get the linearized equations for the perturbations. When projected on the invariant manifold the linearized equations for the perturbations are:

$$\frac{dc}{dt} = -\mu c + m(\beta/m^2 - U^e)s - mS^e v, \quad (\text{A2a})$$

$$\frac{ds}{dt} = -\mu s - m(\beta/m^2 - U^e)c - (\eta_0 - mC^e)v, \quad (\text{A2b})$$

$$\frac{dv}{dt} = -\mu v + \frac{1}{2}\eta_0 s, \quad (\text{A2c})$$

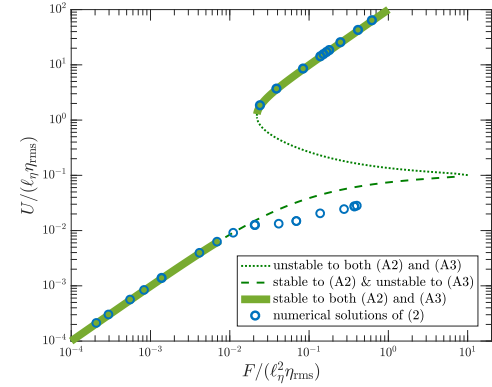


FIG. A1. The steady solutions (7) for topography η^{\parallel} and their stability as predicted by (A2) and (A3). Also shown with circles are the numerical solutions of (2) for comparison.

The orthogonal complement of the linearized equations reads:

$$\begin{aligned} \nabla^2 \phi_t &= -[(U^e \nabla^2 + \beta) \partial_x + \mu \nabla^2] \phi - \left\{ [S^e \cos(mx) \right. \\ &\quad \left. - C^e \sin(mx)] (\nabla^2 + m^2) + m \eta_0 \sin(mx) \right\} \phi_y. \end{aligned} \quad (\text{A3})$$

Eigenanalysis of (A2) determines the stability of steady state (7) to perturbations within the invariant manifold; eigenanalysis of (A3) determines the stability of (7) to perturbations outside the manifold.

The eigenanalysis of (A2) is straightforward and has been studied extensively (Hart 1979; Pedlosky 1981; Källén 1982; Rambaldi and Flierl 1983; Yoden 1985). However, the novel eigenanalysis of (A3) is worth some extra comments. First note that if ϕ is independent of y , i.e. $\phi_y = 0$, (A3) implies stability. Therefore, a necessary condition instability of (A3) is $\phi_y \neq 0$. In this case, note that

- (i) (A3) is homogeneous in y , i.e. if $\phi(x, y, t)$ is a solution so is $\phi(x, y + a, t)$ for any a ,
- (ii) the coefficients of (A3) remain unchanged under $x \rightarrow x + 2\pi\kappa/m$ for any integer κ , i.e. if $\phi(x, y, t)$ is a solution so is $\phi(x + 2\pi\kappa/m, y, t)$.

Thus, we can search for the eigensolutions $\phi = e^{\lambda_n t} \hat{\phi}_n(x, y)$ with $\mathbf{n} \stackrel{\text{def}}{=} (n_x, n_y)$ and $\hat{\phi}_n(x, y)$ a single harmonic in y and a Bloch eigenfunction in x , $\hat{\phi}_n = e^{in_y y} \tilde{\phi}_{n_x}(x)$ with $n_y \neq 0$ and

$$\tilde{\phi}_{n_x} \stackrel{\text{def}}{=} e^{in_x x} \sum_{M=-\infty}^{+\infty} c_M e^{iMmx}. \quad (\text{A4})$$

In (A4) the zonal Bloch wavenumber, n_x , is restricted within the first Brillouin zone, $|n_x| \leq m/2$. Therefore, for each meridional wavenumber n_y the stability of (A3) reduces to the eigenvalue problem:

$$\lambda_n \nabla_{n_y}^2 \tilde{\phi}_{n_x} = L_{n_y} \tilde{\phi}_{n_x}, \quad (\text{A5})$$

where $\nabla_{ny}^2 \stackrel{\text{def}}{=} \partial_x^2 - n_y^2$ and

$$\mathcal{L}_{ny} \stackrel{\text{def}}{=} -[(U^e \nabla_{ny}^2 + \beta) \partial_x + \mu \nabla_{ny}^2] - i n_y \left\{ [S^e \cos(mx) - C^e \sin(mx)] (\nabla_{ny}^2 + m^2) + m \eta_0 \sin(mx) \right\}.$$

By inserting (A4) in (A5) the eigenproblem reduces into an infinite system of equations with unknowns the coefficients c_M and eigenvalue λ_n . Truncating the sum of (A4) up to $|M| \leq M_{\max}$ gives us $2M_{\max} + 1$ equations for $2M_{\max} + 2$ unknowns: $c_{-M_{\max}}, c_{-M_{\max}+1}, \dots, c_{M_{\max}}$ and λ_n . These equations can be compactly written as:

$$\mathbf{A}(\lambda_n) \begin{bmatrix} c_{-M_{\max}} \\ \vdots \\ c_{M_{\max}} \end{bmatrix} = 0, \quad (\text{A6})$$

where \mathbf{A} is a $(2M_{\max} + 1) \times (2M_{\max} + 1)$ matrix. A non-trivial solution of (A6) exists only when $\det[\mathbf{A}(\lambda_n)] = 0$, and this condition determines the eigenvalues λ_n that correspond to the eigenfunction with wavevector \mathbf{n} (Lorenz 1972).

The region of stability of the steady state (7) for the topography η^{\parallel} is marked with the thick semitransparent curve in figure 2(a), both for the lower- and in the upper-flow regime. It is found that the lower-branch solution first become unstable to perturbations that lie outside the invariant manifold i.e., instability is first triggered by (A3) rather than by (A2). Figure A1 shows the stability of (7) as predicted by (A2) and (A3) together with the numerical results of (2) for comparison.

The stability calculations presented in this Appendix assume that the topography does not depend on y . However, the same flow transitions occur in the presence of complex topography with open geostrophic contours. In that case, finding the lower- and upper-branch equilibrium steady states is much more painful since some of the Jacobian terms, for example $J(\psi^e, \eta)$, are *not* identically zero. Therefore, the lower- and upper-branch solutions do not lie within any low-dimensional manifold. Methods for obtaining such equilibria were developed by Tung and Rosenthal (1985).

References

- Abernathey, R., and P. Cessi, 2014: Topographic enhancement of eddy efficiency in baroclinic equilibration. *J. Phys. Oceanogr.*, **44** (8), 2107–2126, doi:10.1175/JPO-D-14-0014.1.
- Arbic, B. K., and G. R. Flierl, 2004: Baroclinically unstable geostrophic turbulence in the limits of strong and weak bottom Ekman friction: Application to midocean eddies. *J. Phys. Oceanogr.*, **34** (10), 2257–2273, doi:10.1175/1520-0485(2004)034<2257:BUGTIT>2.0.CO;2.
- Böning, C. W., A. Dispert, M. Visbeck, S. R. Rintoul, and F. U. Schwarzkopf, 2008: The response of the Antarctic Circumpolar Current to recent climate change. *Nat. Geosci.*, **1** (1), 864–869, doi:10.1038/ngeo362.
- Bracegirdle, T. J., E. Shuckburgh, J.-B. Sallee, Z. Wang, A. J. S. Meijers, N. Bruneau, T. Phillips, and L. J. Wilcox, 2013: Assessment of surface winds over the Atlantic, Indian, and Pacific Ocean sectors of the Southern Ocean in CMIP5 models: historical bias, forcing response, and state dependence. *J. Geophys. Res.-Atmospheres*, **118** (2), 547–562, doi:10.1002/jgrd.50153.
- Carnevale, G. F., and J. S. Frederiksen, 1987: Nonlinear stability and statistical mechanics of flow over topography. *J. Fluid Mech.*, **175**, 157–181, doi:10.1017/S002211208700034X.
- Charney, J. G., and J. G. DeVore, 1979: Multiple flow equilibria in the atmosphere and blocking. *J. Atmos. Sci.*, **36**, 1205–1216, doi:10.1175/1520-0469(1979)036<1205:MFEITA>2.0.CO;2.
- Constantinou, N. C., and W. R. Young, 2016: Beta-plane turbulence above monoscale topography. *J. Fluid Mech.*, URL <https://arxiv.org/abs/1612.03374>, (sub judice, arXiv:1609.06769).
- Cox, S. M., and P. C. Matthews, 2002: Exponential time differencing for stiff systems. *J. Comput. Phys.*, **176** (2), 430–455, doi:10.1006/jcph.2002.6995.
- Davey, M. K., 1980: A quasi-linear theory for rotating flow over topography. Part 1. Steady β -plane channel. *J. Fluid Mech.*, **99** (02), 267–292, doi:10.1017/S0022112080000614.
- Donohue, K. A., K. L. Tracey, D. R. Watts, M. P. Chidichimo, and T. K. Chereskin, 2016: Mean Antarctic Circumpolar Current transport measured in Drake Passage. *Geophys. Res. Lett.*, **43**, 11 760–11 767, doi:10.1002/2016GL070319.
- Farneti, R., T. L. Delworth, A. J. Rosati, S. M. Griffies, and F. Zeng, 2010: The role of mesoscale eddies in the rectification of the Southern Ocean response to climate change. *J. Phys. Oceanogr.*, **40**, 1539–1557, doi:10.1175/2010JPO4353.1.
- Farneti, R., and Coauthors, 2015: An assessment of Antarctic Circumpolar Current and Southern Ocean meridional overturning circulation during 1958–2007 in a suite of interannual CORE-II simulations. *Ocean Model.*, **93**, 84–120, doi:10.1016/j.ocemod.2015.07.009.
- Firing, Y. L., T. K. Chereskin, and M. R. Mazloff, 2011: Vertical structure and transport of the Antarctic Circumpolar Current in Drake Passage from direct velocity observations. *J. Geophys. Res.-Oceans*, **116** (C8), C08015, doi:10.1029/2011JC006999.
- Hallberg, R., and A. Gnanadesikan, 2001: An exploration of the role of transient eddies in determining the transport of a zonally reentrant current. *J. Phys. Oceanogr.*, **31** (11), 3312–3330, doi:10.1175/1520-0485(2001)031<3312:AEOTRO>2.0.CO;2.
- Hallberg, R., and A. Gnanadesikan, 2006: The role of eddies in determining the structure and response of the wind-driven Southern Hemisphere overturning: Results from the modeling eddies in the Southern Ocean (MESO) project. *J. Phys. Oceanogr.*, **36**, 2232–2252, doi:10.1175/JPO2980.1.
- Hart, J. E., 1979: Barotropic quasi-geostrophic flow over anisotropic mountains. *J. Atmos. Sci.*, **36** (9), 1736–1746, doi:10.1175/1520-0469(1979)036<1736:BQGFOA>2.0.CO;2.
- Hogg, A. M., M. P. Meredith, J. R. Blundell, and C. Wilson, 2008: Eddy heat flux in the Southern Ocean: Response to variable wind forcing. *J. Climate*, **21**, 608–620, doi:10.1175/2007JCLI1925.1.
- Hogg, A. M., M. P. Meredith, D. P. Chambers, E. P. Abrahamsen, C. W. Hughes, and A. K. Morrison, 2015: Recent trends in the Southern

- Ocean eddy field. *J. Geophys. Res.-Oceans*, **120**, 1–11, doi:10.1002/2014JC010470.
- Holloway, G., 1987: Systematic forcing of large-scale geophysical flows by eddy-topography interaction. *J. Fluid Mech.*, **184**, 463–476, doi:10.1017/S0022112087002970.
- Johnson, G. C., and H. L. Bryden, 1989: On the size of the Antarctic Circumpolar Current. *Deep-Sea Res.*, **36** (1), 39–53, doi:10.1016/0198-0149(89)90017-4.
- Källén, E., 1982: Bifurcation properties of quasigeostrophic, barotropic models and their relation to atmospheric blocking. *Tellus*, **34** (3), 255–265, doi:10.1111/j.2153-3490.1982.tb01814.x.
- Kassam, A.-K., and L. N. Trefethen, 2005: Fourth-order time-stepping for stiff PDEs. *SIAM J. Sci. Comput.*, **26** (4), 1214–1233, doi:10.1137/S1064827504210633.
- Lorenz, E. N., 1972: Barotropic instability of Rossby wave motion. *J. Atmos. Sci.*, **29**, 258–269, doi:10.1175/1520-0469(1972)029<0258:BIORWM>2.0.CO;2.
- Mak, J., D. P. Marshall, J. R. Maddison, and S. D. Bachman, 2017: Emergent eddy saturation from an energy constrained parameterisation. *Ocean Model.*, **112**, 125–138, doi:10.1016/j.ocemod.2017.02.007.
- Marshall, D. P., M. H. P. Abbaum, J. R. Maddison, D. R. Munday, and L. Novak, 2017: Eddy saturation and frictional control of the Antarctic Circumpolar Current. *Geophys. Res. Lett.*, **44**, doi:10.1002/2016GL071702.
- Marshall, D. P., J. R. Maddison, and P. S. Berloff, 2012: A framework for parameterizing eddy potential vorticity fluxes. *J. Phys. Oceanogr.*, **42**, 539–557, doi:10.1175/JPO-D-11-048.1.
- Marshall, G. J., 2003: Trends in the Southern Annular Mode from observations and reanalyses. *J. Climate*, **16**, 4134–4143, doi:10.1175/1520-0442(2003)016<4134:TITSAM>2.0.CO;2.
- Masich, J., T. K. Chereskin, and M. R. Mazloff, 2015: Topographic form stress in the Southern Ocean State Estimate. *J. Geophys. Res.-Oceans*, **120** (12), 7919–7933, doi:10.1002/2015JC011143.
- Meredith, M. P., A. C. Naveira Garabato, A. M. Hogg, and R. Farneti, 2012: Sensitivity of the overturning circulation in the Southern Ocean to decadal changes in wind forcing. *J. Climate*, **25**, 99–110, doi:10.1175/2011JCLI4204.1.
- Morisson, A. K., and A. M. Hogg, 2013: On the relationship between Southern Ocean overturning and ACC transport. *J. Phys. Oceanogr.*, **43**, 140–148, doi:10.1175/JPO-D-12-057.1.
- Munday, D. R., H. L. Johnson, and D. P. Marshall, 2013: Eddy saturation of equilibrated circumpolar currents. *J. Phys. Oceanogr.*, **43**, 507–532, doi:10.1175/JPO-D-12-095.1.
- Munk, W. H., and E. Palmén, 1951: Note on the dynamics of the Antarctic Circumpolar Current. *Tellus*, **3**, 53–55, doi:10.1111/j.2153-3490.1951.tb00776.x.
- Nadeau, L.-P., and R. Ferrari, 2015: The role of closed gyres in setting the zonal transport of the Antarctic Circumpolar Current. *J. Phys. Oceanogr.*, **45**, 1491–1509, doi:10.1175/JPO-D-14-0173.1.
- Nadeau, L.-P., and D. N. Straub, 2009: Basin and channel contributions to a model Antarctic Circumpolar Current. *J. Phys. Oceanogr.*, **39** (4), 986–1002, doi:10.1175/2008JPO4023.1.
- Nadeau, L.-P., and D. N. Straub, 2012: Influence of wind stress, wind stress curl, and bottom friction on the transport of a model Antarctic Circumpolar Current. *J. Phys. Oceanogr.*, **42** (1), 207–222, doi:10.1175/JPO-D-11-058.1.
- Nadeau, L.-P., D. N. Straub, and D. M. Holland, 2013: Comparing idealized and complex topographies in quasigeostrophic simulations of an Antarctic Circumpolar Current. *J. Phys. Oceanogr.*, **43** (8), 1821–1837, doi:10.1175/JPO-D-12-0142.1.
- Pedlosky, J., 1981: Resonant topographic waves in barotropic and baroclinic flows. *J. Atmos. Sci.*, **38** (12), 2626–2641, doi:10.1175/1520-0469(1981)038<2626:RTWIBA>2.0.CO;2.
- Peña Molino, B., S. R. Rintoul, and M. R. Mazloff, 2014: Barotropic and baroclinic contributions to along-stream and across-stream transport in the Antarctic Circumpolar Current. *J. Geophys. Res.-Oceans*, **119** (11), 8011–8028, doi:10.1002/2014JC010020.
- Rambaldi, S., and G. R. Flierl, 1983: Form drag instability and multiple equilibria in the barotropic case. *Il Nuovo Cimento C*, **6** (5), 505–522, doi:10.1007/BF02561449.
- Rintoul, S. R., S. Sokolov, M. J. M. Williams, B. Peña Molino, M. Rosenberg, and N. L. Bindoff, 2014: Antarctic Circumpolar Current transport and barotropic transition at Macquarie Ridge. *Geophys. Res. Lett.*, **41** (20), 7254–7261, doi:10.1002/2014GL061880.
- Straub, D. N., 1993: On the transport and angular momentum balance of channel models of the Antarctic Circumpolar Current. *J. Phys. Oceanogr.*, **23**, 776–782, doi:10.1175/1520-0485(1993)023<0776:OTTAAM>2.0.CO;2.
- Swart, N. C., and J. C. Fyfe, 2012: Observed and simulated changes in the Southern Hemisphere surface westerly wind-stress. *Geophys. Res. Lett.*, **39** (16), L16 711, doi:10.1029/2012GL052810.
- Tansley, C. E., and D. P. Marshall, 2001: On the dynamics of wind-driven circumpolar currents. *J. Phys. Oceanogr.*, **31**, 3258–3273, doi:10.1175/1520-0485(2001)031<3258:OTDOWD>2.0.CO;2.
- Thompson, A. F., and A. C. Naveira Garabato, 2014: Equilibration of the Antarctic Circumpolar Current by standing meanders. *J. Phys. Oceanogr.*, **44** (7), 1811–1828, doi:10.1175/JPO-D-13-0163.1.
- Thompson, D. W. J., and S. Solomon, 2002: Interpretation of recent Southern Hemisphere climate change. *Science*, **296**, 895–899, doi:10.1126/science.1069270.
- Tung, K.-K., and A. J. Rosenthal, 1985: Theories of multiple equilibria – A critical reexamination. Part I: Barotropic models. *J. Atmos. Sci.*, **42**, 2804–2819, doi:10.1175/1520-0469(1985)042<2804:TOMEAC>2.0.CO;2.
- Ward, M. L., and A. M. Hogg, 2011: Establishment of momentum balance by form stress in a wind-driven channel. *Ocean Model.*, **40** (2), 133–146, doi:10.1016/j.ocemod.2011.08.004.
- Yang, X.-Y., R. X. Huang, and D. X. Wang, 2007: Decadal changes of wind stress over the Southern Ocean associated with Antarctic ozone depletion. *J. Climate*, **20** (14), 3395–3410, doi:10.1175/JCLI4195.1.
- Yoden, S., 1985: Bifurcation properties of a quasi-geostrophic, barotropic, low-order model with topography. *J. Meteor. Soc. Japan. Ser. II*, **63** (4), 535–546.